Strike-slip restraining screwed fault geometry reconstructed from the 2025 Myanmar earthquake

Dye SK Sato[1], Ryo Okuwaki[2], Yuji Yagi[2], and Yukitoshi Fukahata[3]

[1]Research Institute for Marine Geodynamics, Japan Agency for Marine-Earth Science and Technology, Kanagawa, Japan

[2]Institute of Life and Environmental Sciences, University of Tsukuba, Ibaraki, Japan

[3]Disaster Prevention Research Institute, Kyoto University, Kyoto, Japan

Key Points:

- A fault surface of the 2025 Myanmar earthquake is reconstructed based on the potency density tensor inversion of teleseismic P-waves
- Restraining fault twists are detected around the fault-segment junctions that suspended rupture episodes of the earthquake
- The estimated fault shape explains along-strike dip-angle variations observed in the focal mechanism that reflects P-wave polarity

Corresponding author: Daisuke Sato, `daisukes@jamstec.go.jp`

Abstract

We present a fault surface model of the 2025 Mw 7.7 Myanmar earthquake based on the potency density tensor inversion (PDTI) of teleseismic P-waves combined with surface reconstruction from distributed potency tensor solutions. Our source model demonstrates that the earthquake fault is twisted, varying the dip angle along strike. Inferred fault twists are prominent near fault-segment junctions, around which respective rupture episodes are shown reflected and arrested. Those obtained underground fault images are warranted by the polarity of teleseismic P-waves sensitive to dip-angle variations. Since the reconstructed fault twists, which fit interseismic geodetic surveys, have the potential to restrain rupture propagations, geometrical irregularities detected around segment junctions provide a consistent explanation of why this earthquake nearly halted several times.

Plain Language Summary

On 28 March 2025, a moment-magnitude 7.7 earthquake occurred in the Sagaing Region, Myanmar. Its nationwide strong ground motions demonstrate the extreme length of the source region that crosses the nation. This study reconstructs this stretched fault surface through a seismological analysis. In our model, the fault rupture propagation was suspended several times at the locations previously broadly envisioned, but the rupture restarted each time until breaching the entire source region. Moreover, our analysis revealed that the source fault is twisted around the points of those rupture suspensions. Although those twists are geometrical anomalies exceptional in the mature and well-continuous Sagaing fault system that hosted the earthquake, they are consistent with geodetic surveys conducted before the earthquake, which locate the junctions of faults. Because fault twists can restrain fault ruptures, it is likely that the twists of the faults in the underground, prominent enough to create topographical irregularities that segment the faults, have nearly halted the rupture propagation. The 2025 Myanmar earthquake provides an important example that fault geometry can restrain earthquake ruptures as forecast, but does not necessarily arrest them.

1 Introduction

The 2025 Myanmar earthquake struck central Myanmar on March 28, 2025. The earthquake source is a right-lateral faulting of Mw 7.7 with the epicenter at 22.011°N, 95.936°E (USGS, 2025). Its slip zone is situated in the southern Sagaing fault system,

which is an active continental transform fault system driven by the strain partitioning from the India-Sunda oblique convergence (Wang et al., 2014; Steckler et al., 2016). In particular, the Meiktila (MTL) segment around 20°N–21.4°N, one of the main rupture zones of this earthquake (Mai et al., 2025), has been regarded as a seismic gap that itself should experience a rock failure given its long-lasting quiescence (Hurukawa & Maung Maung, 2011).

However, the earthquake rupture has propagated further south after breaching the seismic gap, and the rupture process extending over 400 km is more complex than expected (Mai et al., 2025; Inoue et al., 2025; Melgar et al., 2025). The rupture history consists of three rupture episodes (Inoue et al., 2025): the first episode that ruptures the Sagaing (SG) segment, the second episode that ruptures the MTL segment, and the third episode that ruptures the Nay Pyi Taw (NPT) segment, which also slightly ruptures the Pyu (PYU) segment. The spatial correlation between the rupture episodes and fault segments suggests the influence of fault geometry on the rupture process, also manifested as the epicenter location near a pull-apart basin that concentrates stress loads interseismically (Xiong et al., 2017; Aung, 2025). Nevertheless, quantitative discussion on fault geometry has been difficult because even the geodetic observations that have been extensively conducted in the Sagaing fault system leave a high degree of uncertainty regarding the underground fault geometry (Tin et al., 2022). In terms of data residuals of finite fault inversions, the fault shape suggested by geodetic observations is not necessarily supported by the seismic waveforms of this earthquake (Melgar et al., 2025), even though the fault nonplanarity is likely (Inoue et al., 2025; Ye et al., 2025).

A clue to the shape of underground faults may lie in seismic information on the earthquake focal mechanism. Besides the less attenuating nature of seismic waves, vertically radiated teleseismic waves are sensitive to vertical tilts of earthquake mechanisms, including dip angles of strike-slip faults, thus complementary to geodetic and geological surveys sensitive to horizontal information near the ground (Okuwaki et al., 2020). Nonplanar fault geometry inference from the seismic focal mechanism is enabled by the inference of distributed focal mechanisms (Kikuchi & Kanamori, 1991), known as potency density tensor inversion (PDTI; Shimizu et al., 2020). We have recently developed a method to translate the distributed beachballs of focal mechanisms into a three-dimensional fault surface (Sato et al., 2025). By integrating this method with the updated framework of
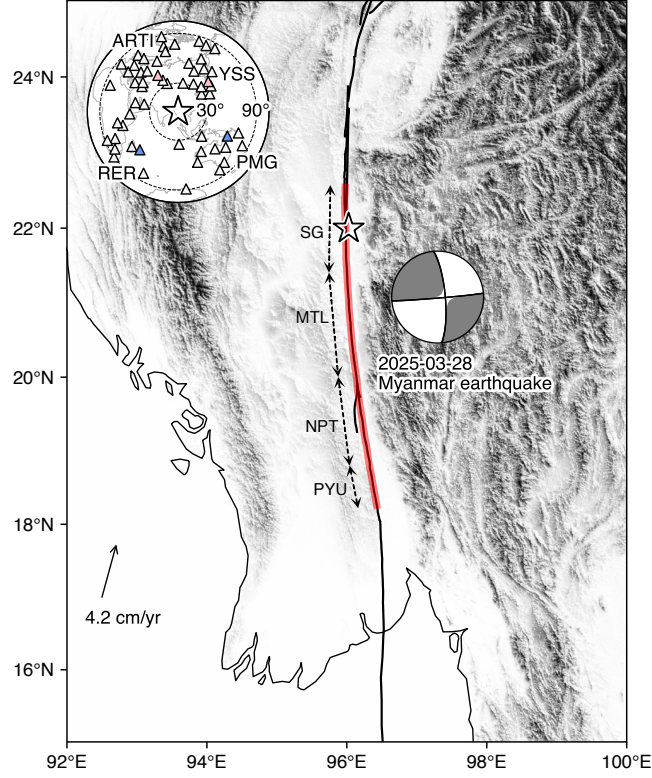
Figure 1. Overview of the study region. The source information is shown in the epicenter (USGS, 2025, the star), the seismic moment (the beachball), and the fault trace (Reitman et al., 2025, the red curve). The tectonic setting is profiled by active faults (Styron et al., 2010, the black lines), fault segments (Tin et al., 2022, the dotted arrows), and the relative plate motion (DeMets et al., 2010, the solid arrow). The background topography is from GEBCO_2025 Grid (GEBCO Compilation Group, 2025) Selected stations (the triangles) are plotted in the inset circle with the dashed contours of the epicentral distances 30° and 90°. Four stations investigated in the Discussion section (ARTI, YSS, RER, and PMG) are painted as in Fig. 3.

the PDTI (Shimizu et al., 2020, 2021; Yamashita et al., 2022), we attempt to reconstruct the source fault surface of the 2025 Myanmar earthquake.

2 Data and Method

Data selection and processing follow Inoue et al. (2025), in which this earthquake is analyzed by the PDTI. 58 observation stations are selected such that the azimuthal coverage over the source fault is guaranteed (Fig. 1, inset circle). Vertical velocity components of teleseismic P-waves downsampled at 0.7 sec intervals are inverted.

The method of analysis is an updated version of the PDTI (Shimizu et al., 2020, 2021; Yamashita et al., 2022) combined with the fault surface reconstruction from distributed potency tensor beachballs (Sato et al., 2025). We solve the simultaneous inference of potency-density rates and fault geometry by decomposing it into alternate iterations of potency-density-rate inference given fault geometry and fault geometry reconstruction from given potency-density rates (Shimizu et al., 2021). The PDTI using fixed fault geometry is solved by a stable scheme of Shimizu et al. (2020) that follows the method of Yagi & Fukahata (2011), accounting for Green's function error propagation to the model parameters. The time-adaptive smoothing over space and time is further incorporated as a prior constraint upon the potency-density rate (Yamashita et al., 2022). The PDTI simultaneously evaluates the scales of variances for observation and Green's function errors and smoothing factors of the prior constraint in line with Akaike's Bayesian information criterion (ABIC; Akaike, 1980; Yabuki & Matsu'ura, 1992). Fault surface reconstruction from the potency density is solved by the method of Sato et al. (2025), which enables three-dimensional surface reconstruction from distributed potency. Only the part of the surface reconstruction is different from the analysis of Inoue et al. (2025).

The potency density provides a field of normal vectors, and normal vectors in turn describe infinitesimal motions along the fault surface by a partial differential equation. Its solution, the reconstructed fault, depends on the boundary condition, namely the constraint on fault edges that include the on-ground fault trace (Sato et al., 2025). This study has employed two types of fault-edge boundary conditions during surface reconstruction based on the solutions in Sato et al. (2025). The first is a free-end boundary condition imposing nothing on the fault edges ('the baseline solution' in Sato et al., 2025). Here, the rigid-body translation of a fault, unconstrained from normal vectors, is removed from an additional constraint that the fault passes through the hypocenter. The second is the rigid-end boundary condition imposed along the fault trace, which is expressed by an L2 norm penalty on the deviation from the nominal fault trace; the remaining edges are free-ended in this constraint. The associated constraint is hereafter termed 'shallow elevation damping'. We have expressed the nominal fault trace as a straight line that tracks the reference plane, considering the maturity of the Sagaing fault system resulting in its on-ground flatness (Fig 1). The motivation here is to investigate how well the seismically constrained fault shape agrees with the surface observations. This study does not use the observed fault trace as explicit a priori information.

118   In the implementation, the model space is spanned along a reference plane of 540

119   km strike and 31.5 km dip passing through the hypocenter at the origin, oriented by 355°

120   strike and 90° dip based on the GCMT solution (Dziewonski et al., 1981; Ekström et al.,

121   2012). The spatial convolution between Green's function and the potency-density rate

122   is collocated on the fault surface with collocation points taken every 12 km along reference-

123   plane strike and every 4.5 km along reference-plane dip. We employ theoretical point-

124   source Green's functions calculated from the one-dimensional structure of the ak135 model (Ken-

125   nett et al., 1995; Montagner & Kennett, 1996) with linear-piecewise bases of 0.1 sec in-

126   tervals. Our analysis prohibits rupture propagation speeds above 6 km/sec from the hypocen-

127   ter. The hypocenter of USGS (2025) is located west of the fault and does not match the

128   polarity of eastward dipping (Fig. 1), and so the epicenter in our inversion has been shifted

129   0.1° eastward from the nominal hypocenter 21.996°N, 95.926°E in Inoue et al. (2025).

3 Results

131   Our optimal source model, denoted by the baseline solution in Data and Method,

132   is summarized in Fig. 2. The moment rate function that spatially integrates the moment

133   density rate indicates three peaks corresponding to respective episodes of the earthquake

134   (Fig. 2a). According to the reconstructed fault, the southern Sagaing fault system host-

135   ing the 2025 Myanmar earthquake forms a screwed geometry that rotates clockwise as

136   it heads south (Fig. 2a, b). The estimated dip angle abruptly changes around episode

137   boundaries approximately 70 and 210 km south of the epicenter at 22°N (Fig. 2c, d), which

138   are in agreement with the locations of segment junctions (SG-MTL and MTL-NPT at

139   21.4 and 20 °N, respectively). The latter phase of the third episode approximately from

140   75 sec produces two fast-slipping zones partitioned around 340 km south of the epicen-

141   ter (Fig. 2c), analogous to the NPT-PYU junction at 18.8 °N.

142   Due to the abrupt dip-angle changes around segment junctions, the respective re-

143   constructed fault segments have their own dip angles. In the estimated beachballs of as-

144   sociated time ranges (Fig. 2a), the SG segment, which hosted the first episode, has a dip

145   angle of approximately 60 degrees, while the MTL segment, which hosted the second episode,

146   has a dip of approximately 80 degrees. In the third episode that ruptures the NPT and

147   PYU segments, the NPT segment is slightly west-dipping with dip angles (Fig. 2a, b),

148   as detected in the beachballs of 75-85 sec (Fig. 2c), whereas the PYU segment starting

149   around 18.8°N is east dipping (Fig. 2a). The focal mechanism of the entire third episode
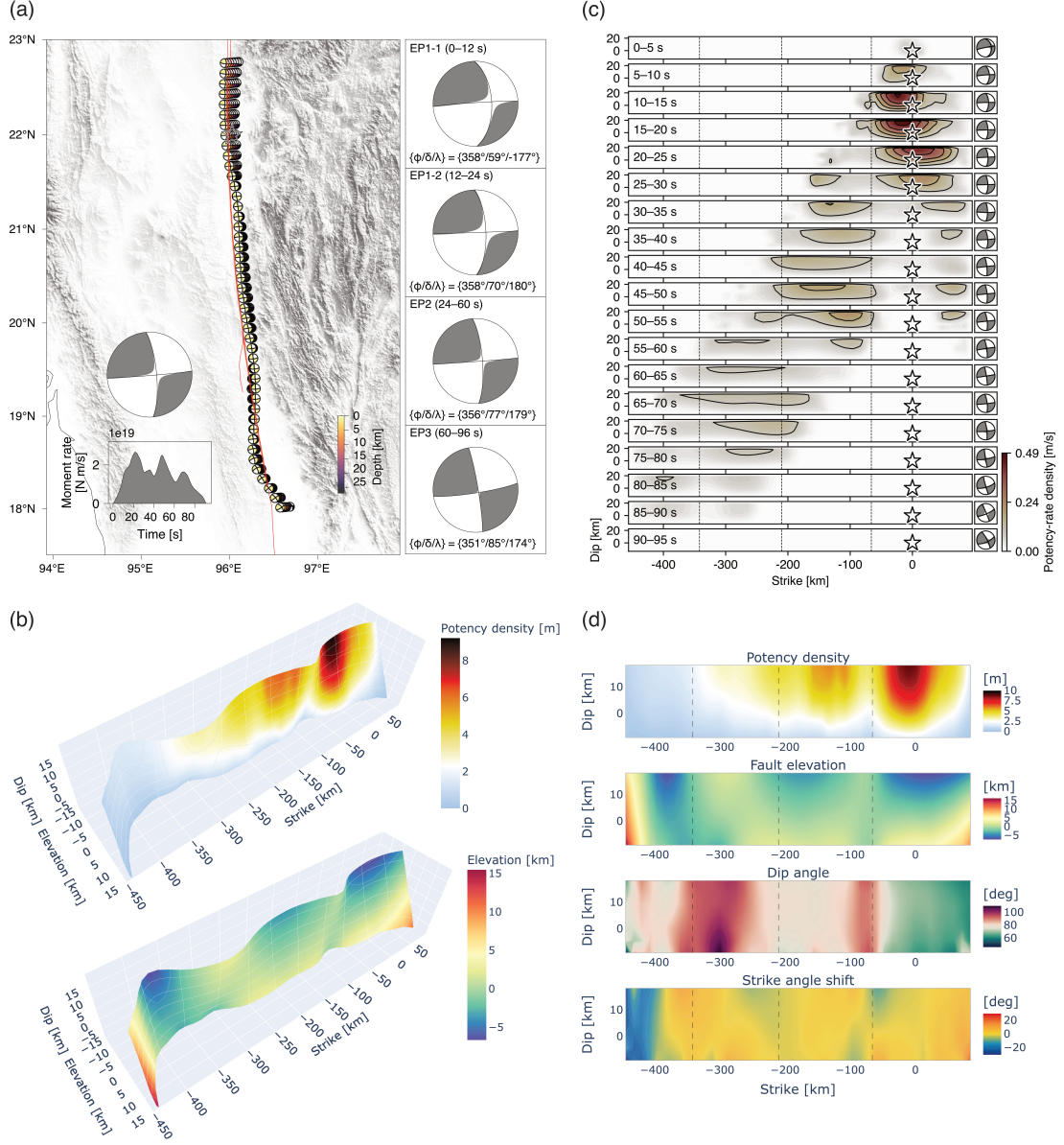
Figure 2. The optimal source model. The fault reconstruction procedure follows the baseline solution of Sato et al. (2025). (a) Distributed potency tensors with the moment rate function and the beachball of the entire moment. Moment beachballs of four time ranges and their strike ϕ, dip δ, and rake λ angles are also computed from space-time integrals of potency-density rates. The epicenter (the star) and the traces of the source fault (Reitman et al., 2025, transparent red) and active faults (Styron et al., 2010, thick red) are drawn for comparison. (b) Perspective view of the potency density on the reconstructed fault. The fault elevation is measured against a vertical reference plane of a 355-degree strike angle passing through the hypocenter at the origin. (c) Snapshots of the potency rate density fields and spatially averaged potency tensors. The vertical lines represent partitions of the first to third and potential fourth episodes located 66, 210, and 342 km away from the hypocenter (the stars) in reference-strike distance. (d) Potency density, fault elevations, and strike and dip angles plotted on a reference plane. Plotted strike angles show the deviations from the reference strike. The vertical partitions follow Fig. 2c.

in Fig. 2a has a dip angle of approximately 85 degrees, possibly as a superposition of the slight west-dipping of the NPT and the east-dipping of the PYU, but the east-dipping of the PYU segment may be unsure given the insignificant amount of potency in this zone (Fig. 2b).

The strike angle also weakly varies along strike (Fig. 2a). The strike trend is broadly westward convex. The parabolic strike variations in the SG segment form a bowl-shaped fault scarp, consistent with the remarkable east-dipping of that segment. Slight eastward protrusions are detected near the segment junctions that divide the rupture episodes (Fig. 2a, d), although to be precise, those protrusions are dip-angle features that locally vary dip angles rather than strike (Fig. 2d). Such weak variations in strike, vague in the rotation of the potency beachballs, are relatively clearly captured in the reconstructed surface.

Snapshots of potency-density rates illustrate that the characteristic locations of rupture propagations, such as rupture initiations, reflections, and terminations, are almost always located around segment junctions (Fig. 2c). In all episodes, the rupture front propagation suspends around the junctions. Cessations of reflected fast-slipping zones also occurred around the junction in the first and second episodes, although the third episode stopped at the segment center. Meanwhile, the nominal timing of rupture initiation varies depending on the episode sectioning, making quantitative discussion difficult. Nonetheless, the second and third episodes appear to have branched off from the preceding episodes at the timing when they were reflected at junctions (15–20 sec and 50–55 sec, Fig. 2c).

The eastward protrusions near the junctions act as restraining bends that inhibit right-lateral strike slips regardless of the propagation direction, functioning as barriers for both southward and northward rupture propagations of this earthquake. The abrupt dip changes around junctions also have the potential to act as strike-slip restraining twists, as underground sigmoidal bends produced by fault twists can restrain strike-slip ruptures. Those geometrical barriers reconstructed around segment junctions, where the rupture episodes began, reflected, and stopped, collectively imply the influence of fault geometry upon the earthquake complexity.

The above series of results are, however, potentially related to a flaw of the model that the reconstructed fault does not fully match the fault trace (transparent red line in Fig. 2a). This trace mismatch may reflect abrupt geometrical variations near the ground, or rather, may come from data sensitivity issues of the PDTI, where the far-field wave-

182 forms are more sensitive to dip angles than strike. In the following Discussion section,
183 we make a minor modification in surface reconstruction to assess how the surface fault
184 mismatch affects the results.

4 Discussion

186 By exploiting the three-dimensional surface reconstruction method by Sato et al.
187 (2025), our seismological analysis was able to reconstruct a fault surface consistent with
188 the rupture process of the 2025 Myanmar earthquake. Other than the previously uncon-
189 structed fault surface, our source model is consistent with previous studies of this earth-
190 quake, including slip zones of high potency densities correlated with fault segments re-
191 ported in finite fault inversions (Mai et al., 2025; Melgar et al., 2025). The estimated po-
192 tency beachballs (Fig. 2a) are not largely shifted from the PDTI of Inoue et al. (2025)
193 obtained without fault surface reconstruction. The reconstructed screwed geometry also
194 agrees with the geometrical features estimated from the interseismic campaign observa-
195 tions (Tin et al., 2022). The consistencies between our source model and previous stud-
196 ies reinforce our results.

197 Because the fault surface obtained from interseismic geodetic data (Tin et al., 2022)
198 is left unresolved by the waveform residuals of finite fault inversions (Melgar et al., 2025),
199 it would be worth investigating why our analysis detects fault nonplanarity. Figure 3 is
200 a comparison of the double-couple beachball diagram between the first episode (Fig. 3
201 left) and the episode summation (Fig. 3 right). Four observation points (ARTI, YSS, RER,
202 and PMG) that cover the four quadrants of the total seismic moment near their lower-
203 hemisphere intersection are superimposed on the beachballs. Among those four, the first-
204 episode polarities, corresponding to the initial-motion, at YSS and PMG located in the
205 right two quadrants of the total beachball have different polarities from those quadrants.
206 Namely, a planar fault conforming to the total moment cannot explain those near-nodal
207 polarities of initial P-waves. This dissonance between the initial and total mechanisms
208 is the primary data that demonstrates the reconstructed fault nonplanarity of the left-
209 handed screw fault, which rotates its dip while moving the rupture zone southward over
210 time (Fig. 2c). A similar support is found in the multiple point source analysis of Ye et
211 al. (2025), where the focal mechanisms of episodes indicate screwing rotations. One po-
212 tential cause of the aforementioned conclusion in Melgar et al. (2025) is that the fault
213 shape of Tin et al. (2022) is based on a rough approximation connecting the surface fault
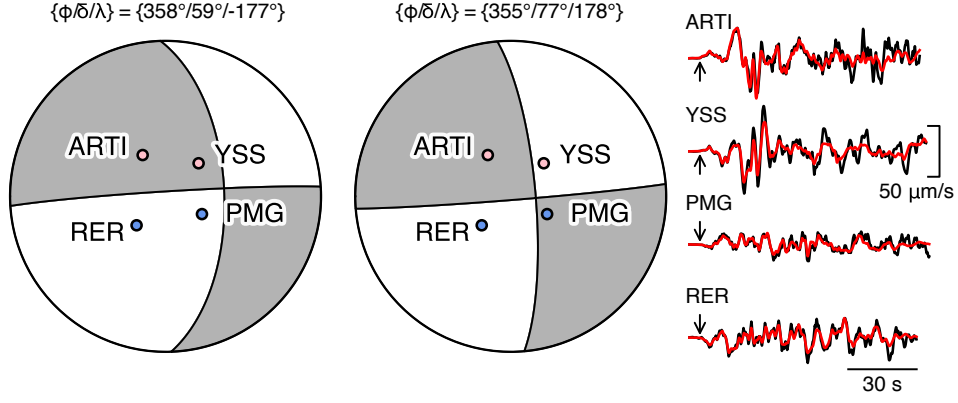
Figure 3. Beachball comparison between the double-couple components of the first episode (left) and the episode summation (right). Their strike ϕ, dip δ, and rake λ angles are also calculated. Four stations painted in the inset circle of Fig. 1, ARTI, YSS, RER, and PMG, are superimposed on the two beachballs. The station colors represent the polarities of initial motions (pink: upward; blue: downward). The associated waveforms are drawn for comparison (red: modeled; black: observed).

214 and an anti-plane point dislocation under the assumption of fault segment planarity, the

215 reconstructed fault of which may not significantly improve the P-wave polarity explain-

216 ability from a planar vertical fault; we should here note that geodetic data are based on

217 fast-attenuating elastostatic deformations not advantageous for constraining underground

218 geometry (Segall, 2010). Another potential cause is that data residuals could be reduced

219 by the overfitting of slip patterns to data, thus perhaps not sensitive to fault shape. Since

220 the sensitivity of seismic-wave polarity to fault orientations has been established in point-

221 source modeling (Dziewonski et al., 1981), distributing those geometrical features of an

222 earthquake fault (Kikuchi & Kanamori, 1991) may rationalize our nonplanar fault re-

223 construction.

224   Insufficient consistency between the estimated fault shape and the surface fault re-

225 mains an issue. To mitigate this mismatch, we try out appending the constraint on the

226 fault trace into our analysis (Fig. 4). Deviations from a planar surface shape are penal-

227 ized by the L2 norm (shallow elevation damping in Data and Method), the weight of which

228 (α) is a tuning parameter, selected to bring the reconstructed fault trace close to the ex-

229 pected fault trace, here set at $\alpha = 0.07$; in our analysis, a small penalty ($\alpha < 0.03$)

230 results in the same shape as the above-mentioned baseline solution (Fig. 2a) and a large
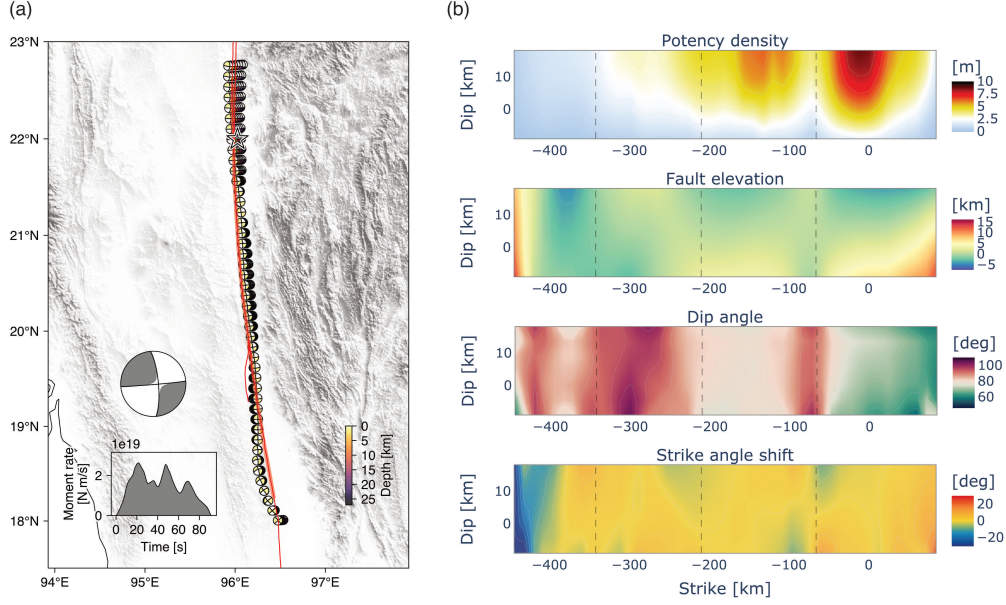
Figure 4. An alternative source model accounting for fault trace flatness. The fault reconstruction procedure follows shallow elevation damping in Data and Method. (a) Bird's-eye view of the distributed potency tensors. The visualization scheme follows Fig. 2a. (b) Potency density, fault elevations from a vertical reference plane, and strike and dip angles plotted on a reference plane. The vertical partitions follow Fig. 2c.

penalty ($\alpha > 0.1$) results in an almost completely flat line, so the parameter tuning of α is not relevant. This minor modification of the surface reconstruction results in a flatter fault trace better aligning with the observed fault trace. The shallowest beachballs overlap with active faults except for the area south of the NPT-PYU junction at 18.8 °N (Fig. 4a), in which the PDTI lacks accuracy due to insignificant potency in that zone. Even after this modification flattening the shallow portion, dip-angle variations remain, whereas along-strike bends around junctions become weaker (Fig. 4b). The eastward protrusions at junctions that vary both dip and strike angles persist (Fig. 4a). The relevant and robust shape characteristics of the reconstructed source fault are therefore considered along-strike dip-angle variations of a twisted fault.

The results of our inverse analysis suggest that the earthquake was nearly halted by geometrical anomalies of fault segments but those geometrical barriers (Das & Aki, 1977; Aki, 1979) were not sufficient to terminate the momentum of the strain release. The rupture continuation after breaching the seismic gap may challenge existing seis-

mic hazard assessments (Melgar et al., 2025). Physics-based considerations on rupture arrests (e.g., Finzi & Langer, 2012; Bruhat et al., 2016; Lozos, 2021; Zhang et al., 2022; Ozawa et al., 2023) would be necessary to more quantitatively incorporate geometrical effects into hazard assessments. Compared to the role of two-dimensional fault nonplanarity as restraining and releasing bends (Sibson, 1985; Kase & Day, 2006; Mann, 2007; Biasi & Wesnousky, 2017, 2021), the role of three-dimensional twists is less understood, and the mechanical influence of the detected screwed geometry upon the earthquake rupture awaits future scrutiny. Lozos (2021) performs dynamic rupture simulations of smooth nonplanar strike-slip faults and finds that fault twists can induce rupture arrests irrespective of twist direction relative to slip and propagation directions, interpreting it from the twist-induced obliqueness from preferred fault orientations and the crack-tip energy imbalance caused by the change in the rupture propagation direction. Zhang et al. (2022) exactly find the correlation between rupture segmentation and abrupt dip-angle changes in their earthquake sequence modeling of the Yingxiu-Beichuan fault in southwestern China. Such physics of smoothly twisted faults provides a reasonable explanation for our results, while the geometrical irregularities we found are located around fault-segment junctions, which may not be mechanically modeled by a smooth fault. Multiple segmented, torn fault surfaces also explain sudden changes in dip angles as well as rupture episode arrests around junctions (Wesnousky, 2006; Finzi & Langer, 2012; Biasi & Wesnousky, 2016). The validity of those scenarios would eventually be measured by paleoseismic records on the earthquake cycle, where the same-sized earthquake has been documented as a possible event in 1839 (Hurukawa & Maung Maung, 2011). The earthquake this time reaffirms that fault segments observed in topography and paleoseismicity are important clues in assessing the maximal size of the fault rupture.

5 Conclusions

We have reconstructed the source fault surface of the 2025 Myanmar earthquake by analyzing teleseismic P-waves. The performed PDTI analysis involving surface reconstruction was able to reveal the underground fault structures unconstrained in previous studies, thanks to the high sensitivity of the teleseismic waves to the tilts of strike-slip faults. Our optimal source model concludes that the earthquake fault is screwed, rotating clockwise as it heads south. Screwed dip-angle variations are shown to be significant around segment junctions, where the fault is also shown to protrude eastward. Those

segment junctions of geometrical irregularities have produced a major part of the initiations, reflections, and terminations of rupture episodes. Therefore, although the earthquake did not stop when breaching the seismic gap correlated to a fault segment, it appears likely that geometrical anomalies of segment boundaries contributed to the arrests of those rupture episodes. Further mechanical considerations are necessary to understand the causality between twisted fault geometry and rupture suspensions and to deepen hazard assessments from the seismically elucidated fault geometry. A fully objective estimation of the three-dimensional earthquake fault would be an important advance in earthquake source inversion.

Open Research Section

Waveform data are downloaded from the Seismological Facility for the Advancement of Geoscience Data Management Center via the EarthScope Consortium Wilber 3 system (https://ds.iris.edu/wilber3/) and processed in Inoue et al. (2025). The ground topography in the paper refers to GEBCO_2025 Grid (GEBCO Compilation Group, 2025). The plate motion is from MORVEL2010 (DeMets et al., 2010). Active faults and the fault trace are based on Styron et al. (2010) and Reitman et al. (2025).

Acknowledgments

References

Akaike, H. (1980). *Likelihood and the Bayes procedure, in "Bayesian Statistics", ed. by jm bernardo, mh degroot, dv lindley, and afm smith.* University Press, Valencia.

Aki, K. (1979). Characterization of barriers on an earthquake fault. *Journal of Geophysical Research: Solid Earth*, *84*(B11), 6140–6148.

Aung, H. H. (2025). The supershear earthquake (M 7.7) in Mandalay, Myanmar on 28th March 2025. *Archives of Current Research International*, *25*(6), 473–478.

Biasi, G. P., & Wesnousky, S. G. (2016). Steps and gaps in ground ruptures: Empirical bounds on rupture propagation. *Bulletin of the Seismological Society of America*, *106*(3), 1110–1124.

Biasi, G. P., & Wesnousky, S. G. (2017). Bends and ends of surface ruptures. *Bulletin of the Seismological Society of America*, *107*(6), 2543–2560.

Biasi, G. P., & Wesnousky, S. G. (2021). Rupture passing probabilities at fault bends and steps, with application to rupture length probabilities for earthquake early warning. *Bulletin of the Seismological Society of America*, *111*(4), 2235–2247.

Bruhat, L., Fang, Z., & Dunham, E. M. (2016). Rupture complexity and the supershear transition on rough faults. *Journal of Geophysical Research: Solid Earth*, *121*(1), 210–224.

Das, S., & Aki, K. (1977). Fault plane with barriers: A versatile earthquake model. *Journal of geophysical research*, *82*(36), 5658–5670.

DeMets, C., Gordon, R. G., & Argus, D. F. (2010). Geologically current plate motions [Dataset]. *Geophysical journal international*, *181*(1), 1–80.

Dziewonski, A. M., Chou, T.-A., & Woodhouse, J. H. (1981). Determination of earthquake source parameters from waveform data for studies of global and regional seismicity. *Journal of Geophysical Research: Solid Earth*, *86*(B4), 2825–2852.

Ekström, G., Nettles, M., & Dziewoński, A. M. (2012). The global CMT project 2004–2010: Centroid-moment tensors for 13,017 earthquakes. *Physics of the Earth and Planetary Interiors*, *200*, 1–9.

Finzi, Y., & Langer, S. (2012). Predicting rupture arrests, rupture jumps and cascading earthquakes. *Journal of Geophysical Research: Solid Earth*, *117*(B12).

GEBCO Compilation Group. (2025). *GEBCO 2025 Grid.* doi: 10.5285/37c52e96-24ea-67ce-e063-7086abc05f29

Hurukawa, N., & Maung Maung, P. (2011). Two seismic gaps on the Sagaing Fault, Myanmar, derived from relocation of historical earthquakes since 1918. *Geophysical Research Letters*, *38*(1).

Inoue, N., Yamaguchi, R., Yagi, Y., Okuwaki, R., Enescu, B., & Tadapansawut, T. (2025, May). A multiple asymmetric bilateral rupture sequence derived from the peculiar tele-seismic P-waves of the 2025 Mandalay, Myanmar earthquake. *Seismica*, *4*(1). Retrieved from https://seismica.library.mcgill.ca/article/view/1691 doi: 10.26443/seismica.v4i1.1691

Kase, Y., & Day, S. (2006). Spontaneous rupture processes on a bending fault. *Geo-*

physical Research Letters, *33*(10).

Kennett, B. L., Engdahl, E., & Buland, R. (1995). Constraints on seismic veloc-ities in the Earth from traveltimes. *Geophysical Journal International*, *122*(1), 108–124.

Kikuchi, M., & Kanamori, H. (1991). Inversion of complex body waves—III. *Bulletin of the Seismological Society of America*, *81*(6), 2335–2350.

Lozos, J. C. (2021). The effect of along-strike variation in dip on rupture propaga-tion on strike-slip faults. *Geosphere*, *17*(6), 1616–1630.

Mai, P. M., Li, B., Jonsson, S., Suhendi, C., Liu, J., Li, D., . . . Klinger, Y. (2025). Breaching a seismic gap: the 2025 magnitude 7.7 Myanmar earthquake. *Research Square*.

Mann, P. (2007). Global catalogue, classification and tectonic origins of restraining-and releasing bends on active and ancient strike-slip fault systems.

Melgar, D., Weldon, R., Wang, Y., Bato, M. G., Aung, L. T., Shi, X., . . . Dawson, T. (2025, Jul.). Supershear source model of the 2025 M7.8 Myanmar earthquake and paleoseismology of the Sagaing Fault: regions of significant overlap with past earthquakes. *Seismica*, *4*(2). Retrieved from `https://seismica.library.mcgill.ca/article/view/1771` doi: 10.26443/seismica.v4i2.1771

Montagner, J.-P., & Kennett, B. (1996). How to reconcile body-wave and normal-mode reference Earth models. *Geophysical Journal International*, *125*(1), 229–248.

Okuwaki, R., Hirano, S., Yagi, Y., & Shimizu, K. (2020). Inchworm-like source evo-lution through a geometrically complex fault fueled persistent supershear rupture during the 2018 Palu indonesia earthquake. *Earth and Planetary Science Letters*, *547*, 116449.

Ozawa, S., Ando, R., & Dunham, E. M. (2023). Quantifying the probability of rupture arrest at restraining and releasing bends using earthquake sequence simu-lations. *Earth and Planetary Science Letters*, *617*, 118276.

Reitman, N. G., Wang, Y., Kuo, Y.-T., Hanagan, C., Hatem, A. E., DuRoss, C. B., . . . Schmitt, R. G. (2025). *Remote Surface Rupture Observations for the M7.7 2025 Mandalay, Burma (Myanmar) Earthquake [Dataset].* Retrieved from `https://doi.org/10.5066/P1RYMWCK` (U.S. Geological Survey Data Release) doi: 10.5066/P1RYMWCK

Sato, D. S., Yagi, Y., Okuwaki, R., & Fukahata, Y. (2025). Smooth surface reconstruction of earthquake faults from distributed potency beachballs. *arXiv preprint arXiv:2506.14082*.

Segall, P. (2010). Earthquake and volcano deformation. In *Earthquake and volcano deformation*. Princeton University Press.

Shimizu, K., Yagi, Y., Okuwaki, R., & Fukahata, Y. (2020). Development of an inversion method to extract information on fault geometry from teleseismic data. *Geophysical Journal International*, *220*(2), 1055–1065.

Shimizu, K., Yagi, Y., Okuwaki, R., & Fukahata, Y. (2021). Construction of fault geometry by finite-fault inversion of teleseismic data. *Geophysical Journal International*, *224*(2), 1003–1014.

Sibson, R. H. (1985). Stopping of earthquake ruptures at dilational fault jogs. *Nature*, *316*(6025), 248–251.

Steckler, M. S., Mondal, D. R., Akhter, S. H., Seeber, L., Feng, L., Gale, J., . . . Howe, M. (2016). Locked and loading megathrust linked to active subduction beneath the Indo-Burman Ranges. *Nature Geoscience*, *9*(8), 615–618.

Styron, R., Taylor, M., & Okoronkwo, K. (2010). Database of Active Structures From the Indo-Asian Collision [Dataset]. *Eos, Trans. Am. Geophys. Union*, *91*(20), 181–182. Retrieved from `https://agupubs.onlinelibrary.wiley.com/doi/10.1029/2010EO200001` doi: 10.1029/2010EO200001

Tin, T. Z. H., Nishimura, T., Hashimoto, M., Lindsey, E. O., Aung, L. T., Min, S. M., & Thant, M. (2022). Present-day crustal deformation and slip rate along the southern sagaing fault in Myanmar by GNSS observation. *Journal of Asian Earth Sciences*, *228*, 105125.

USGS. (2025). *M 7.7 - 2025 Mandalay, Burma (Myanmar) Earthquake.* `https://www.usgs.gov/news/featured-story/m77-mandalay-burma-myanmar-earthquake`. (Accessed August 7, 2025)

Wang, Y., Sieh, K., Tun, S. T., Lai, K.-Y., & Myint, T. (2014). Active tectonics and earthquake potential of the Myanmar region. *Journal of Geophysical Research: Solid Earth*, *119*(4), 3767–3822.

Wesnousky, S. G. (2006). Predicting the endpoints of earthquake ruptures. *Nature*, *444*(7117), 358–360.

Xiong, X., Shan, B., Zhou, Y., Wei, S., Li, Y., Wang, R., & Zheng, Y. (2017).

Coulomb stress transfer and accumulation on the Sagaing Fault, Myanmar, over the past 110 years and its implications for seismic hazard. *Geophysical Research Letters*, *44*(10), 4781–4789.

Yabuki, T., & Matsu'ura, M. (1992). Geodetic data inversion using a bayesian information criterion for spatial distribution of fault slip. *Geophysical Journal International*, *109*(2), 363–375.

Yagi, Y., & Fukahata, Y. (2011). Introduction of uncertainty of Green's function into waveform inversion for seismic source processes. *Geophysical Journal International*, *186*(2), 711–720.

Yamashita, S., Yagi, Y., Okuwaki, R., Shimizu, K., Agata, R., & Fukahata, Y. (2022). Potency density tensor inversion of complex body waveforms with time-adaptive smoothing constraint. *Geophysical Journal International*, *231*(1), 91–107.

Ye, L., Lay, T., & Kanamori, H. (2025). The 28 March 2025 Mw 7.8 Myanmar Earthquake: Preliminary Analysis of an 480 km Long Intermittent Supershear Rupture. *The Seismic Record*, *5*(3), 260–269.

Zhang, L., Liu, Y., Li, D., Yu, H., & He, C. (2022). Geometric control on seismic rupture and earthquake sequence along the Yingxiu-Beichuan fault with implications for the 2008 Wenchuan earthquake. *Journal of Geophysical Research: Solid Earth*, *127*(12), e2022JB024113.